coatings

MDPI

Article

Enhanced Wear Behavior of a Stainless Steel Coating Deposited on a Medium-Carbon Low-Alloy Steel Using Ultrasonic Impact Treatment

Li Li [1,2], Shudong Guo [3], Lu Jia [1], Li Zhang [4], Jiangang Li [5], Xigang Wang [1], Nannan Zhang [6], Hongyan Gan [7], Yanhui Guo [8] and Suyan Zhao [9,10,*]

1 Department of Mechanical Engineering, Taiyuan Institute of Technology, Taiyuan 030008, China; lili03039@mail.dlut.edu.cn (L.L.); jialu19890812@126.com (L.J.); wxg8151105@sina.com (X.W.)
2 State Key Laboratory of Structural Analysis for Industrial Equipment, Department of Engineering Mechanics, Dalian University of Technology, Dalian 116024, China
3 Taian Quality and Technical Inspection and Testing Institute, Taian 271000, China; gsd0905@163.com
4 Shanxi Culture Relics Bureau, Taiyuan 030000, China; zjy168_ssll@163.com
5 China New Energy Development (Zhejiang) Co., Ltd., Hangzhou 310000, China; a0351@139.com
6 Department of Material Science and Engineering, Shenyang University of Technology, Shenyang 110870, China; zhangnn@sut.edu.cn
7 College of Mechanical Engineering, Shenyang Polytechnic College, Shenyang 110045, China; ganhongyan@126.com
8 Nuclear and Radiation Safety Center, Beijing 100082, China; guoyh2005@163.com
9 Natural Resource Asset Capital Research Center, Hebei GEO University, Shijiazhuang 050031, China
10 School of Management, Hebei GEO University, Shijiazhuang 050031, China
* Correspondence: zsy800605@hgu.edu.cn

Abstract: This study aims to explore the effects of ultrasonic impact parameters on the surface modification of a stainless steel coating deposited on a medium-carbon low-alloy steel using argon arc surfacing welding. Ultrasonic impact treatment (UIT), at three different vibration strike numbers (40,000 times/(mm^2), 57,600 times/(mm^2), and 75,000 times/(mm^2)) marked UIT–1, UIT–2, and UIT–3, respectively, was carried out to modify the surface structure and properties of the stainless steel coating. The surface morphological and structural features, phase compositions, grain size, topography, micro-mechanical properties, as well as the wear resistance of the coating before and after UIT with different impact parameters were experimentally investigated. The results of optical microscopy (OM), scanning electron microscopy (SEM), electron backscatter diffraction (EBSD), and X-ray diffraction (XRD) analyses revealed that the grain refinement accompanied by the formation of the strain-induced α'–martensite occurred on the UIT-treated coating surface. With the increase in the vibration strike number, the surface grain size and roughness decreased, while the α'–martensite content increased. Micro-hardness after UIT was increased by about 19% (UIT–1), 39% (UIT–2), and 57% (UIT–3), and the corresponding wear rate obtained was decreased by 39%, 72%, and 85%, respectively. Significant improvements in wear resistance were achieved using UIT. However, an excessive vibration strike number on the per unit area (/mm^2) might result in unwanted micro-cracks and delamination on the treated surface, deteriorating the performance of the coating. These findings validate that UIT parameters (such as the vibration strike number on per unit area) are of great importance to bringing about improvements in wear performance, and UIT is found to have a high potential in modifying the surface characteristics and optimizing the mechanical performances of the deposited coating for a wide range of potential applications.

Keywords: surfacing welding; coating; ultrasonic impact treatment; wear resistance; wear mechanism

Citation: Li, L.; Guo, S.; Jia, L.; Zhang, L.; Li, J.; Wang, X.; Zhang, N.; Gan, H.; Guo, Y.; Zhao, S. Enhanced Wear Behavior of a Stainless Steel Coating Deposited on a Medium-Carbon Low-Alloy Steel Using Ultrasonic Impact Treatment. *Coatings* **2023**, *13*, 2024. https://doi.org/10.3390/coatings13122024

Academic Editor: Michał Kulka

Received: 27 September 2023
Revised: 20 November 2023
Accepted: 23 November 2023
Published: 30 November 2023

1. Introduction

As one of the key parts of diesel engines, camshaft is inevitably subjected to changes in extrusion stress and friction from the tappet; therefore, it is prone to wear during the service process, greatly affecting the performance and life of diesel engines. As far as different kinds of bearings, sealing valves, etc., are concerned, common failure modes are also related to wear, which significantly decreases the serviceability limit and the effective utilization of these components [1–3]. Previous studies have suggested that most wear failures of valves and bearings, usually originating or initiating on their surface and gradually propagating to the interior, are sensitive to surface performance and microstructure [4,5]. Generally, excellent surface wear resistance can effectively improve the surface durability of substrate materials in a desirable way and be obtained by means of coating and deposition technologies, such as physical and chemical vapor deposition [6], electro-deposition [7], laser cladding [8], thermal spraying [9], surfacing [10], and so on. As an effective coating technology, surfacing has a stronger designability in terms of coating chemical composition, high cladding efficiency, low dilution rate and cost, good applicability, and large-scale interface with excellent metallurgical binding to the substrate. To date, surfacing has been widely applied in gears, gear shafts, various valves, etc., to repair worn surfaces or manufacture coatings with excellent properties on vulnerable valve surfaces for wear protection. Deposited coatings with a dense microstructure and outstanding surface properties can considerably decrease wear failure risks and effectively prolong the serving life of these components.

According to their chemical composition, commonly used wear-resistant surfacing materials essentially include five classification groups: iron-based alloys, cobalt-based alloys, nickel-based alloys, copper-based alloys, and tungsten carbides [11–13]. Compared with other surfacing materials, iron-based alloys, showing distinct advantages such as a simple process, little pollution, low cost, high impact and wear resistance, and good weldability and processability, have been widely used in surfacing applications [14,15]. The desired performance of the deposited coating can be achieved through adjusting the composition of iron-based alloy surfacing materials within a wide range. The excellent wear resistance of an iron-based surfacing coating is largely dependent upon the kind, quantity, size, morphology, and distribution of the hard phase (carbide or boride) contained in the coating. So far, a variety of iron-based wear-resistant alloys have been developed and manufactured, namely Fe–Cr–C, Fe–Cr–B, Fe–Cr–B–C, Fe–Cr–C–V, Fe–Cr–W–V–B, Fe–Cr–Mo–B, Fe–C–Cr–Nb–B, and Fe–Mn–Cr–Mo–V [16]. However, due to the steep thermal gradient resulting from the heating of a highly concentrated heat source and its subsequent cooling, welding tensile stress and deformation are inevitable during surfacing. The existence of tensile stress decreases the tensile load capacity, affects the dimension and utilization of the components in some strict situations, and even initiates a micro-crack between the deposited layer and the substrate. Therefore, subsequent post-weld treatment after surfacing is desperately desired.

To achieve further enhancements in surface performance, surface treatment techniques, such as laser shock processing (LSP) [17], mechanical shot peening (MSP) [18], machine hammer peening (MHP) [19], shot peening (SP) [20,21], surface mechanical attrition treatment (SMAT) [22], and ultrasonic impact treatment (UIT) [23,24], have been put forward and attracted considerable attention in various surface protection applications. These methods can provide the treated materials with superior mechanical properties by contributing to refining grain, improving hardness, prompting phase transformation, generating work hardening, changing surface topography, inducing residual compressive stress, and restraining the crack initiation of the treated materials. Among these different approaches, UIT, based on severe plastic deformation and unrestricted by materials, geometric dimension, form feature, and the application situation of the treated material and component, shows significant advantages in terms of its simple equipment, easy operation, low utilization and maintenance costs, larger residual compressive stress, better process controllability, and a more uniformly treated surface. UIT is considered to be the most

economic and effective process, particularly in the case of welded parts and components to eliminate residual stress [25,26], fabricate composite coatings with gradient structure, enhance the bonding strength at the interface between the coating/weld and substrate, improve fatigue resistance, and prolong service life [27,28]. UIT processing is very similar to traditional ultrasonic shot peening but instead of using impact balls, it uses a hemispherical impact needle(s) applied directly to the target materials at a high frequency of more than 20 kHz, so that the substrate is subjected to severe plastic deformation on its surface. Under the repeated high-frequency, high-energy impact of the impact needle(s), sustainably formed severe regional plastic deformation, surface microstructure evolution, and residual compressive stress are introduced in the treated region of the substrate [29,30]. In this case, the desired residual compression stress and deformation can be achieved through adjusting the impact parameters [31].

Up until now, owing to its efficiency, low cost, and minimum geometrical restriction, UIT has been shown to be a very promising technique to use for surface enhancement, and the effects of this on the wear properties of the stainless steel coating have been extensively studied globally. Research on the increased wear resistance of 16MnR steel [30], Ti–6Al–4V alloy [32], 316L stainless steel [24], AZ31B magnesium alloy micro-arc oxidation composite coating [33], and Al0.5CoCrFeMnNi high-entropy alloy coatings [34] induced with UIT has been reported, and many of these studies found that the improvements in wear resistance can be attributed to the following two reasons: the modification of surface topography and the synergistic effects of grain refinement and hardness enhancement. It is more effective to design a coating with a gradient structure in order to achieve excellent tribological properties [11]. Nevertheless, most of these studies focused on the effects of UIT on the surface performances of alloys and metallic substrate, whereas limited research has been devoted to the increased surface modification and strengthening mechanism of coatings induced with UIT. In addition, the information available regarding the application of UIT in surfacing and coating engineering is lacking, even though surfacing has undergone very extensive applications in the manufacture and maintenance of mechanical components. Therefore, evaluating the surface modification of coatings with a high reliability and long service life induced with UIT is an interesting topic and of great significance for exploring the potential domain of UIT, as well as surface protecting and hardening applications.

In light of the challenges described above, this study aims to evaluate the effects of impact parameters on the microstructure, performance, and wear resistance of the surfacing layer deposited on the camshaft. In our previous study [23], a stainless steel coating was deposited and sequentially surface-modified on a low-carbon steel substrate using a combination of argon arc overlaying and UIT technology. Based on these results, the effects of variations in UIT parameters on the surface modification of cladding coatings were further investigated. The relation between the impact parameters and surface microstructure, roughness, micro-mechanical performance, as well as wear resistance obtained from different parameters was experimentally studied in detail. Moreover, the corresponding wear mechanism has also been discussed in terms of the modification of surface morphological and wear properties. This study attempts to elucidate the surface modification of the microstructure and tribological performances of a stainless steel coating subjected to UIT at different parameters, which is of great significance for improving the poor surface wear resistance, especially for these mechanical parts, such as bearings and shafts in automobile, turbine blades, and landing gears in aerospace, where surface properties (especially tribological features) are crucial. The results obtained in this study could contribute to a breakthrough in the limited research on the influences of UIT on the tribological behavior of coatings, a field which expects an exploration of the potential application of UIT for improving surface performance in surface protecting and strengthening engineering.

2. Experimental Procedures

2.1. Materials

A medium-carbon low-alloy structural steel plate, 40Cr (standard GB/T 3077 [35], purchased from Honghuida Commercial and Trading Co. Ltd., Dalian, China, equivalent to 41Cr4 EN ISO 683–1: 2018–09 [36]) was chosen as the substrate, and the chemical composition is outlined in Table 1. Before surfacing, the substrate plate was machined into rectangular samples with dimensions of 100 mm × 100 mm × 10 mm, followed by mechanical grinding and cleaning with acetone on the substrate surface to remove oil and impurities. The surfacing materials used were self-designed multi-component stainless steel flux-cored wires (FCWs), and the chemical composition of the cored powder for the stainless steel FCWs is shown in Table 2. According to the determined chemical composition of the cored powder, raw metal powders were mechanically alloyed in a SX–2 high-energy planetary ball mill (Tianchuang Powder Technology Co., Ltd., Changsha, China), cleaned, filtered, dried, and set aside. The stainless steel FCWs were prepared through filling, compacting, drawing, and rolling sequentially with thin-walled 304 stainless steel seamless pipes employed as the outer skin. The detailed preparation process is outlined in [23].

Table 1. Chemical composition of substrate in weight %.

C	Cr	Ni	Mn	Si	Mo	S	P	Cu	Fe
0.37–0.44	0.8–1.1	<0.3	0.5–0.8	0.17–0.37	<0.1	<0.035	0.035	≤0.25	Bal.

Table 2. Chemical composition of the cored powder for the stainless steel FCWs in weight %.

C	Cr	Ni	Mn	Si	Mo	B	Re	Fe
0.03	<15.5	<8.0	1.0~1.2	0.45~0.55	1.5~2.0	<4.5	<0.05	Bal.

2.2. Surfacing and UIT Experiments

The stainless steel coating was deposited with conventional gas tungsten arc welding (GTAW). Due to the poor weldability of the substrate, a preheating treatment was carried out, and the preheating temperature was kept uniform from start to finish during surfacing. To meet the size requirements of the test specification of the sample preparation, multi-pass surfacing processing was adopted. The detailed surfacing conditions are shown in Table 3.

Table 3. Processing parameters of GTAW.

Parameters	Conditions
Power polarity	Direct current straight polarity (DCSP)
Gas flow (L/min)	12–15
Welding current (A)	150–180
Tungsten diameter (mm)	3.2
Inter-pass temperature (°C)	100–150
Preheat temperature (°C)	~150
Welding speed (mm/min)	80–120

The macroscopic appearance of the cladding coating after surfacing is shown in Figure 1. It can be seen that the deposited coating with a dense structure is well bonded to the substrate. There are no obvious pores, micro-cracks, or other defects observed in the interface between the coating and substrate and its vicinity region. Subsequently, UIT processing was carried out on the deposited coating surface using HY–2050 equipment (manufactured by Shandong Huayun Electromechanical Technology Co., Ltd., Jinan, China), as shown in Figure 2. This UIT equipment mainly consists of an output power supply of approximately 1.5 kW and an ultrasonic generator with a working frequency

of approximately 20 kHz, and the two are connected with a cable. The ultrasonic generator consists of a piezoelectric ceramic transducer, a step-like ultrasonic horn, and a tungsten carbide spherical impact tip mounted on the horn tip. During UIT processing, the ultrasonic oscillator signal generated by the ultrasonic generator is converted into ultrasonic mechanical vibration by the ultrasonic transducer and then amplified using the ultrasonic amplifying rod and transmitted to the impact head. Under the static pressure and high-power ultrasonic drive, the impact head acts directly on the coating surface tens of thousands of strikes per second and moves between the horn tip and the treated coating surface freely.

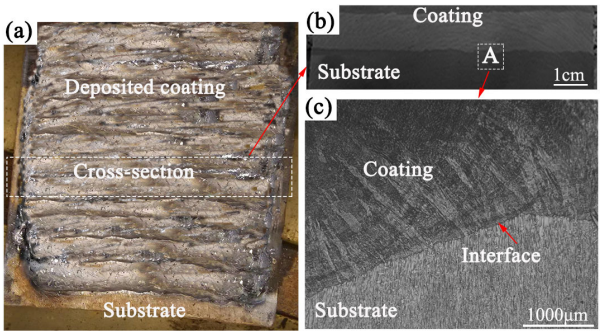

Figure 1. Macro appearances of the coating deposited on the substrate: (**a**) surface morphology; (**b**) cross-sectional morphology; (**c**) magnified image of the selected region A in (**b**).

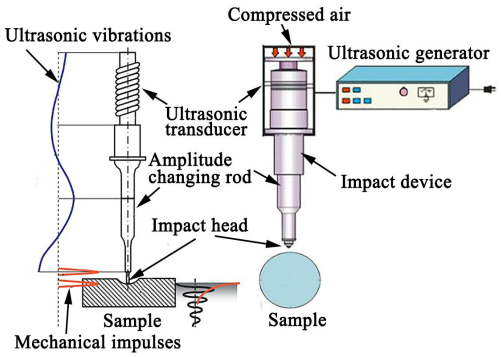

Figure 2. Schematic and instruments of UIT system.

To assure the stability and uniformity of UIT and provide the most reliable impact results, UIT experiments were carried out on a numerical control machine system, as shown in Figure 3. During UIT processing, the impact tip (a tungsten carbide ball with a diameter of 2.38 mm) was attached to the ultrasonic device scans over the coating surface to be treated at a high striking frequency of 20 kHz. A self-designed guideway-sliding block mechanism employed as a positioning and clamping device was fixed to the numerical control machine and controlled the movements of the impact gun along with the impact tip. To obtain effective contact between the impact tip and the coating surface, a constant static load (generally 10 N to 50 N) was applied to the impact tip against the coating surface, driving the impact tip into the coating surface. Considering the synthetic action of impact parameters, such as the static load, amplitude (ranges from 10 to 50 μm), scan speed, and intervals, between neighboring scans on the stability and uniformity of the impact results, "vibration strike numbers N on per unit area (/mm^2)" was applied and taken as the impact parameter indicator. The number of vibration strikes N (in times/mm^2) of the coating surface to be treated relates to the applied ultrasonic frequency f, and the relationship between the two is provided in Equation (1) below.

$$N = \frac{60 \times f}{\upsilon \times S} \quad (1)$$

where υ (in mm/s) is the feed velocity of impact tip and S (in mm/rev) is the feed of the main shaft of the ultrasonic vibratory device. Based on previous findings outlined in [23] and data collected after many attempts, for the sake of generating analysis results accurately and reliably, three groups of impact parameters designated UIT–1, UIT–2, and UIT–3 with different vibration strike numbers were determined, and they are presented in Table 4. The UIT experiment was performed under the condition of a static load of 30 N, and an amplitude of 50 μm was employed.

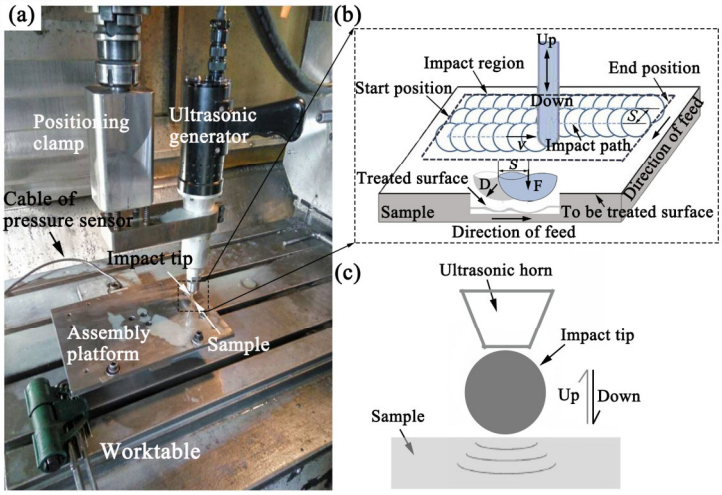

Figure 3. Schematic of ultrasonic impact experiment: (**a**) experimental apparatus; (**b**) diagram of UIT processing; (**c**) simplification of impact tip during UIT.

Table 4. Parameters of UIT processing.

No.	Vibration of Strike Number (Times/mm^2)	Feed Rate S (mm/rev)	Feed Speed ν (m/min)	Time t (min)	Current I (A)
UIT–1	40,000	0.05	36	15	1.4–1.6
UIT–2	57,600		25	25	
UIT–3	75,000		20	45	

2.3. Surface Morphological and Structural Characterization

The cross-sectional microstructure of the samples was observed using optical microscopy (OM, Axio Vert.A1, Carl ZEISS, Jena, Germany) and scanning electron microscopy (SEM, Zeiss Supra 55, Carl Zeiss AG, Oberkochen, Germany) equipped with electron backscatter diffraction (EBSD). The microstructure evolution of the coating surface layer was analyzed using EBSD. The surface phase component and grain size of the coating were investigated using an X-ray diffractometer (Rigaku D/max–2400, Rigaku Corporation, Tokyo, Japan) with Cu–Kα radiation. According to the XRD results, the content of the deformation-induced α′–martensite volume fraction (in vol.%) can be estimated using the direct contrast method, and the average grain size can also be determined based on the Scherrer and Wilsone equation [37,38]. The surface roughness before and after UIT with different parameters was measured using an ET4000A probe roughness profiler (produced by Kosaka Co., Ltd., Tokyo, Japan). During the experiment, surface roughness Ra was measured along three different straight test paths (length about 6 mm) on the coating surface in the width direction using standard [39] and was selected as the assessment indices. The average obtained value of Ra was taken as the result.

2.4. Characterization of Tribological Properties

The friction and wear performances before and after UIT with different parameters was evaluated on an MRH–5A-type tester machine (supplied by Yihua Tribology Testing

Technology Co., Ltd., Jinan, China) under oil-lubricated conditions at room temperature. Figure 4 shows the upper and lower friction counterpart pairs used in the wear experiment. A ring-shaped GCr15 steel with a thickness of 10 mm was employed as the upper friction counterpart pair. The coating samples machined into an annulus with the same thickness were the lower friction counterpart's pair. During the wear test, the upper friction counterpart pair was fixed to the rotation spindle and rotated together with the spindle which was driven by the hydraulic motor at a constant speed. The stationary lower counterpart was closely contacted with the upper friction counterpart and subjected to the applied load from the upper counterpart on their appressed contact interface. The wear test was performed on the appressed contact interface when the upper friction counterparts were driven to rotate by the spindle under the certain test conditions of loads, speed, time, etc. A constant rotation speed of 380 r/min was selected under the different applied loads of 200 N, 400 N, 600 N, 800 N, and 1000 N for 1–5 h, respectively. The lubricating medium used was the ordinary CD40 diesel engine oil (purchased from Jiexuan lubricants Co., Ltd., Guangzhou, China) with a density of about 0.8957 g/cm^3 and a viscosity of 139.6 and 12.5 cSt at 40 and 100 °C, respectively. Before each test, all the specimens were polished and weighed using the electronic balance with an accuracy of 0.0001 g. After the wear tests, the specimens were ultrasonically cleaned, dried, weighed again, and the wear mass loss as well as the wear rate under different conditions were obtained. SEM analysis was used to observe the worn surface morphology and understand the wear mechanism. The detailed testing process has been described elsewhere in [23,40].

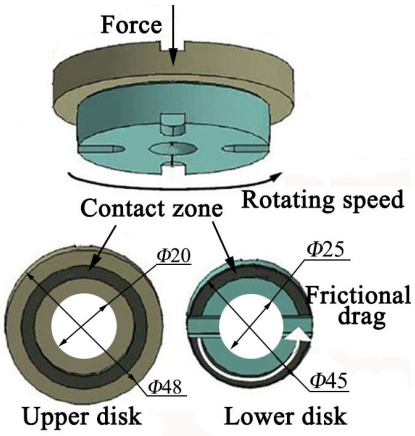

Figure 4. Schematic and dimensions of the ring–ring friction couples of wear tests.

2.5. Characterization of Micro-Mechanical Properties

To reveal the influence of UIT parameters on the micro-mechanical properties of the coating surface, nano-indentation tests were performed on the cross-section using a TI 950 Triboindenter with a Berkovich diamond indenter (Hysitron Inc., Minneapolis, MN, USA). The samples were firstly cross-sectioned along their thickness direction and then impregnated in thermosetting resin, ground with SiC papers, and finally polished. Micro-mechanical properties, including the elastic modulus and micro-hardness of the nine test points (marked as 1, 2, 3, 4, 5, 6, 7, 8, and 9 in red as shown in Figure 5a) with different depths (5 μm, 15 μm, 25 μm, 45 μm, 75 μm, 100 μm, 150 μm, 200 μm, and 250 μm) away from the coating top surface, were measured along the thickness direction, respectively. Considering the nonuniform distribution of the coating structure along its thickness direction, multi-point averaging was applied to improve the measurement precision and prevent calculation failure at the same depth, and the average of 5 adjacent points was taken as the final result. During the test, the maximum load was 1000 μN and the holding time was 20 s. According to the Oliver and Pharr method, the corresponding micro-hardness and elastic modulus were obtained using the recorded load–displacement curves [41].

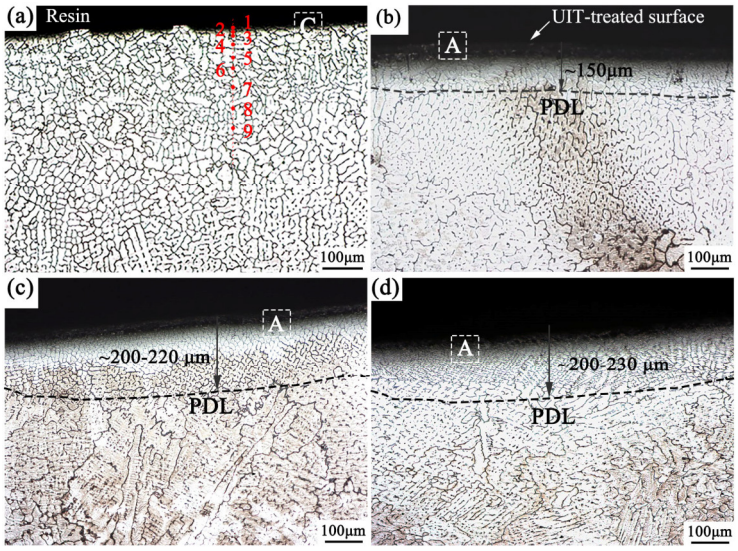

Figure 5. Optical micrograph of cross-section microstructure of near-surface coating: (**a**) before UIT; (**b**) after UIT–1; (**c**) after UIT–2; (**d**) after UIT–3. The selected regions A, C in white dashed box indicate the most top surface layers of the coating.

3. Results and Discussion

3.1. Evolution of Surface Microstructure and Morphology

Figure 5 shows the cross-sectional microstructure before and after UIT with different parameters. Before UIT, the typical equiaxed austenite coarse grains can be observed in the deposited coating surface, as shown in Figure 5a, and the distribution of the grain size was roughly uniform. After UIT, the surface morphology of the coating changed significantly, as shown in Figure 5b–d. Original coarse austenite grains underwent a severe plastic deformation and were distinctly refined. An obvious plastic deformation layer (PDL) with a certain depth was formed on the top surface and naturally transitioned into the coarse grain matrix along the thickness direction. There were no observable boundaries between the plastic deformation layer and the coarse grain matrix. By comparing the microstructure of the UIT-treated coatings with different parameters, it can be found that both the improved refining of the grains and deeper PDL can be achieved at a larger vibration strike number. When N increased from 40,000 times/mm^2 to 57,600 times/mm^2 and 75,000 times/mm^2, the corresponding thickness ranges of PDL were ~150 μm, 220–220 μm, and 200–230 μm, respectively. Clearly, the relationship between the depth of the plastic deformation layer and the vibration strike numbers was not linear. The thickness of PDL increases and gradually reaches stabilization as N increases.

Figure 6 exhibits the higher magnification morphologies of the selected regions (A) on the coating near the surface shown in Figure 5b–d. A thin-layered deformation band structure, several dozens of μm thick, was detected on the topmost coating surface. This layered band structure can be called the fine crystalline layer (FCL), exhibiting obvious rheologic features, where no crystallographic characteristics can be identified. Comparing Figure 6a–c, it is obvious that the grain refinement of the treated samples at a higher strike number outmatched that at a relatively lower strike number. Increasing the vibration strike number N on the per unit area (/mm^2) is favorable for improving grain refinement. The XRD analysis results in the sections that follow have also confirmed this finding. With N increasing from 40,000 times/mm^2 to 57,600 times/mm^2 and 75,000 times/mm^2, the obtained depths of FCL were within certain ranges of ~30 μm, 40–50 μm, and 35–45 μm, respectively. Obviously, the thickness of the fine crystalline layer increased first and then tended to reach saturation even with a slight decline in the vibration strike number. This phenomenon may be related to the work hardening caused by the increased strike number, resulting in the continuous formation of more high-density dislocation. Meanwhile, under the repeated impact, the densely deformed near-surface layer of the treated coating ac-

companied by the continuous refinement of the austenite matrix, the deformation-induced α'–martensitic phase emerged in the austenite matrix due to higher local strains. A similar localized deformation with inhomogeneous high-density dislocation has also been reported regarding the severe plastic deformation processing on 300 series stainless steel [37,42,43] and other materials [44–46]. This will be favorable for improving the wear performance of the coating.

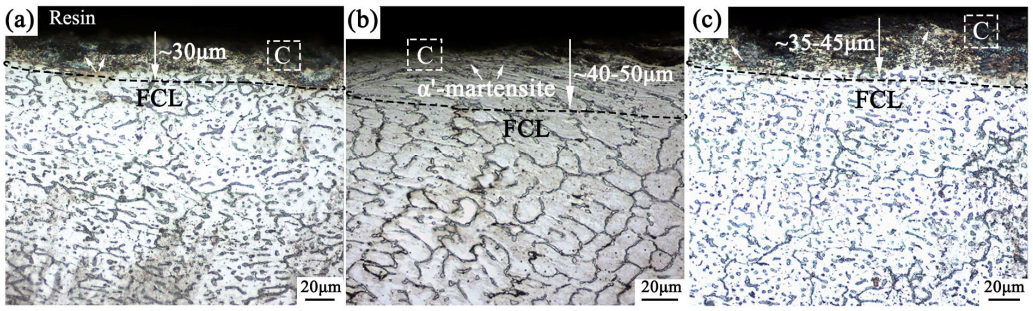

Figure 6. Magnification morphologies of the selected regions (A) shown in Figure 5b–d: (**a**) after UIT–1; (**b**) after UIT–2; (**c**) after UIT–3. White arrows indicate α'–martensite appearance. The selected region C in white dashed box denotes the top surface layers of FCL.

Figure 7 shows the EBSD observation and grain orientation distribution of the selected regions C on the near-surface coating shown in Figures 5a and 6 before and after UIT. As clearly revealed, the initial microstructure of the coating surface was the primary bulky and uneven grain austenitic matrix, showing obvious welding metallurgy solidification characteristics [23], and the grain boundaries were mainly straight and parallel with a preferential orientation. After UIT, an obvious gradient structure distribution can be observed along the thickness direction of the coating, and the minimum grains were mainly distributed over the top surface. The microstructure of the coating surface was composed of ultra-fine equiaxial grains with random orientation. By comparing the surface morphologies with different parameters, it can clearly be seen that the gradient morphologies do change as the vibration strike number N changes on the per unit area. After being treated with UIT–1 (40,000 times/mm), a fine equiaxed grain structure with a certain depth and random orientation distribution was formed on the coating surface. When N increases to 57,600 times/mm^2 (UIT–2), the depth and the random distribution tendency were improved, and the surface average grain size obtained was obviously smaller than that of UIT–1. As N continues to 75,000 times/mm^2 (UIT–3), compared with those of UIT–1 and UIT–2, the depth of the ultra-fine grain layer slightly increased, the grain size dramatically decreased, and the surface microstructure tended to become denser. It can be found that with the vibration strike number N on the per unit area(/mm^2) increasing to a certain range, the grain refinement of the coating surface improved and became gradually stable. The possible reasons for this phenomenon may relate to the grain refinement and the formation of the deformation-induced α'–martensitic phase in the austenite matrix being induced by the repeated impact on the treated regions during UIT processing. It due to the combined effects of grain refinement strengthening and martensitic transformation strengthening that it will be difficult to achieve further plastic deformation and grain refinement, and the ultra-fine grain layer will no longer be deeper but rather reach saturation. If the vibration strike number continues to increase, this will lead to the initiation of microscopic cracks and fractures on the coating surface, deteriorating the performance of the coating instead.

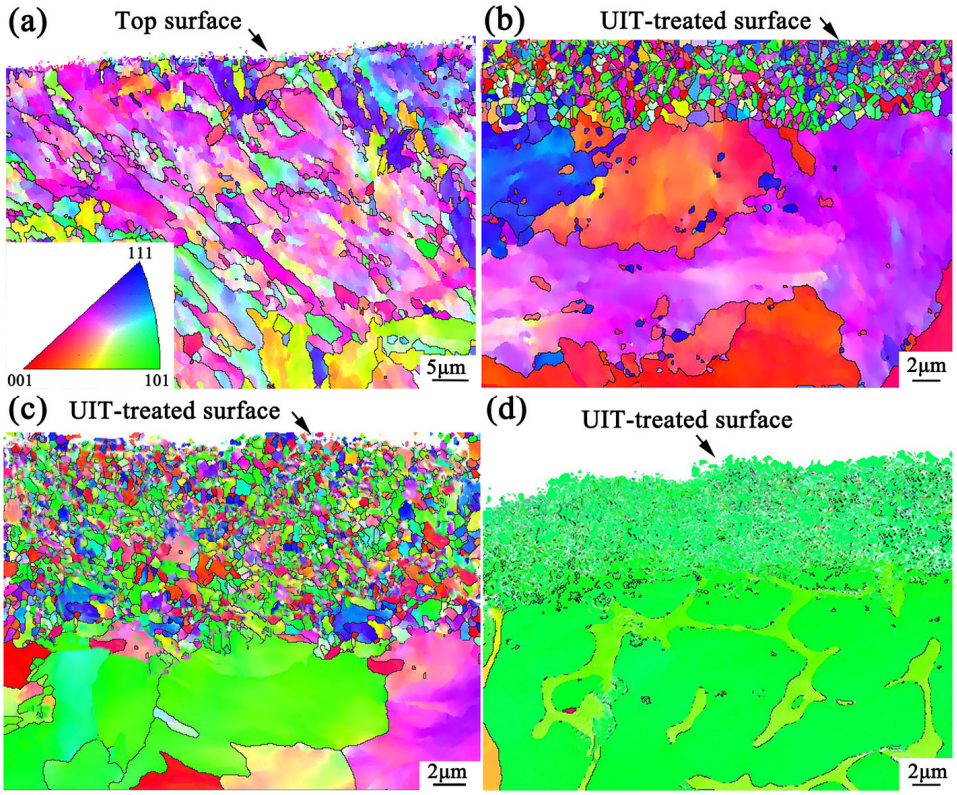

Figure 7. Grain morphologies and orientation distribution of selected region C in near-surface coating: (**a**) before UIT [23]; (**b**) after UIT–1; (**c**) after UIT–2; (**d**) after UIT–3.

3.2. Analysis of XRD Measurement Results

Figure 8 indicates the phase analysis performed on the top surface layer of the coating before and after UIT with different parameters. Before UIT, the phase structure of the deposited coating was evaluated to be mainly face-centered cubic (FCC), which is nearly in single austenitic phase (γ–Fe), accompanying small amounts of other intermetallic dispersed in the austenitic matrix. To clarify the effects of the UIT parameters, only the major phase γ–Fe is taken into account without considering other phases and metallic compounds. From the XRD pattern of the UIT-treated coatings, it was found that compared with the as-deposited coating, the full width at half maximum (FWHM) of the diffraction peaks significantly broadened, and the diffraction peaks intensity decreased significantly. The diffraction peaks corresponded to the martensite phase, with a body-centered cubic (BCC) structure observed in the XRD spectrum. According to a previous study [23], this demonstrates that the austenite grains have been refined, and a certain amount of the deformation-induced α′–martensite phases (α′–Fe) emerged in the austenite matrix. This further validates the veracity of the morphology observations discussed earlier. The formation of the deformation-induced α–martensite can be attributed to the improvements in the hardness and wear resistance of the coating surface. A similar phenomenon was reported in [37,47]. For the UIT-treated coatings, the diffraction peaks are broadened, and the intensity of which tends to become weaker with an increasing vibration strike number. This means that improvements in the grain refinement and α′–Fe content were achieved, along with an increase in the vibration strike number [48,49].

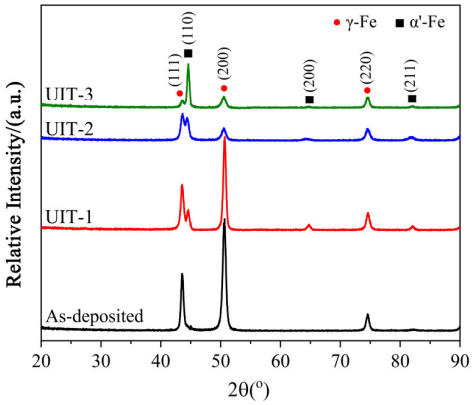

Figure 8. XRD patterns of the coating surface before and after UIT at different impact parameters.

Based on the XRD analysis, the variations in the average grain size and the contents of the deformation-induced α′–martensite of the UIT-treated coating were estimated, and the results are shown in Figure 9. It can be seen that when the vibration strike number increased from 40,000 times/mm^2 (duration about 15 min) to 57,600 times/mm^2 (duration about 25 min) to 75,000 times/mm^2 (duration about 45 min), the average grain size of the top surface was decreased to 120 nm (UIT–1), 80 nm (UIT–2), and 60 nm (UIT–3), respectively. The corresponding content estimation of the α′–Fe in austenite matrix was about 0.087%, 0.136%, and 0.172% in volume fraction. Obviously, when the vibration strike number and time increase, the grain size of the coating surface gradually decreases, even reaching a nanometer scale, while the content of the α′–Fe phase continues to increase. However, an excessive strike number and time may result in microscopic cracks or local damage on the treated coating surface. The appropriate strike numbers and time will be beneficial to attain the desirable properties of the coating.

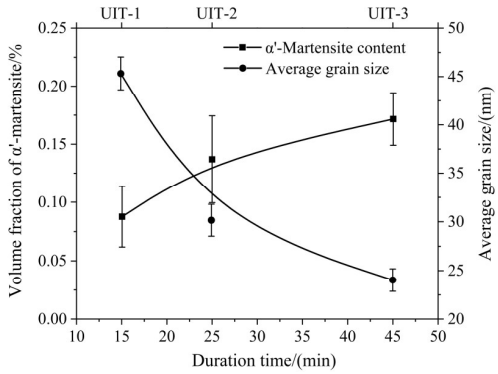

Figure 9. Variations in the average grain size and α′–martensite content of the UIT-treated coating surface.

3.3. Variation in Surface Roughness

Figure 10 shows the surface roughness curves of the coating before and after UIT with different parameters. It is noted that the surface roughness profile of the deposited coating presents an obvious sawtooth shape and irregular distribution. The difference in the vibration amplitudes between the peaks and valleys is great, and the conversion frequency of the two is high. After UIT, the numbers of the peaks/valleys in the roughness curves were significantly reduced within the same tested length, and the difference between the two also decreased. This suggests that the original rough appearance of the deposited coating has been improved under the effects of UIT. Comparing the surface roughness obtained at different impact parameters, it can also be found that the fluctuations of the peaks/valleys in the roughness curves present a weakening trend with the increase in the vibration strike number N per area.

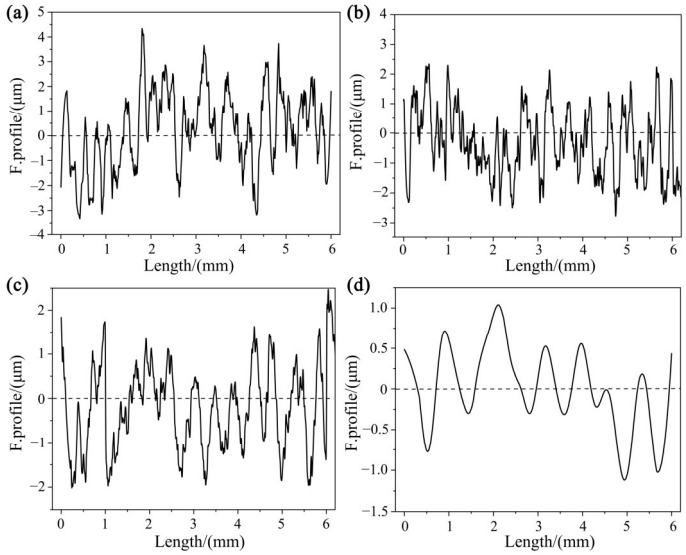

Figure 10. Surface roughness profiles of the coating: (**a**) before UIT; (**b**) after UIT–1; (**c**) after UIT–2; (**d**) after UIT–3.

Figure 11 shows the corresponding average surface roughness (Ra). It can be seen that as the vibration strike number N increased to 40,000 times/mm^2, 57,600 times/mm^2, and 75,000 times/mm^2, the surface roughness decreased from 2.85 (before UIT) to 1.83 (UIT–1), 0.75 (UIT–2), and 0.26 (UIT–3), respectively. Obviously, the surface roughness has been effectively reduced under the effects of UIT. A smooth surface morphology can be achieved by increasing the number of vibration strike N in per unit area. This will be beneficial to improve the surface service performance and fatigue life of the coating.

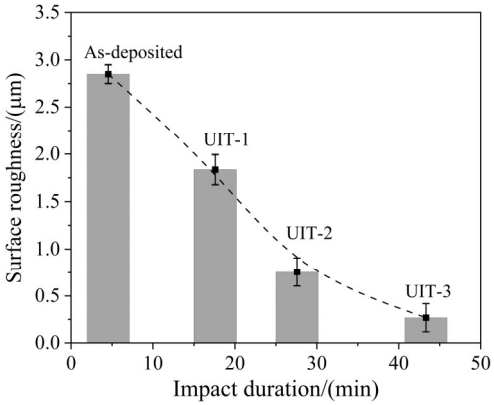

Figure 11. Variation in surface roughness Ra of the coating surface.

3.4. Modification of Micro-Mechanical Properties

Figure 12 shows the load–displacement curves of the selected nine points (P1 corresponding to point 1, P2 to point 2, etc.) on the near-surface coating before and after UIT at different parameters. It can be seen that both the maximum and residual displacements of each test point on the UIT-treated coating surface are smaller than those with the same depth before UIT under the same test conditions. As the number of vibration strike N on the per unit area increased to 40,000 times/mm^2, 57,600 times/mm^2, and 75,000 times/mm^2, the maximum displacements were reduced from 220 nm (before UIT) to 95 nm (UIT–1), 84 nm (UIT–2), and 76 nm (UIT–3), and the corresponding residual displacements obtained decreased from 190 nm to 68 nm, 65 nm, and 60 nm, respectively. The sharp drops in both the maximum and residual displacements indicate that the surface micro-hardness of the UIT-treated coating was considerably higher than that of the coating before UIT.

Obviously, the coating surface was strengthened during UIT processing. By comparing the load–displacement curves shown in Figure 12b–d, it can also be found that by being closer to the impacted top surface within a certain depth range, both the maximum and residual displacements are far smaller than those of other test points far away from the top surface, where the minimum values can be obtained.

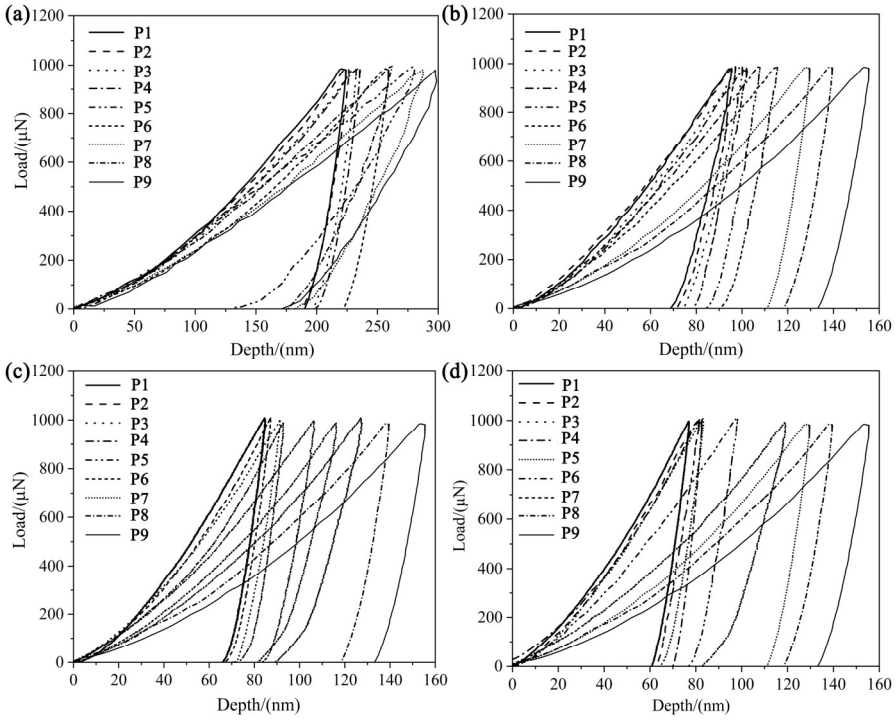

Figure 12. Load–displacement curves of the coating surface: (**a**) before UIT; (**b**) after UIT–1; (**c**) after UIT–2; (**d**) after UIT–3.

The corresponding elastic modulus (Er) and nano-hardness (Hr) of each test point on the coating surface obtained from the nanoindentation measurement are shown in Figure 13. It can be seen that the maximum Er and Hr both occur on the top surface before and after UIT, and the maximum Er and Hr obtained at the same position of the latter are obviously larger than those of the former under the same conditions. The maximum Er and Hr of the coating top surface before UIT are 158 GPa and 4.12 GPa, respectively. After UIT, the maximum Er obtained is 182.59 GPa (UIT–1), 192.89 Gpa (UIT–2), and 210.56 GPa (UIT–3), and the corresponding Hr reached 4.94 GPa, 5.73 GPa, and 6.46 GPa, respectively. Meanwhile, there are striking differences in the distributions of both E_r and H_r between the cladding coating and the UIT-treated coating. Before UIT, despite each point corresponding to a different depth, there were few or not many differences in the distributions of Er and Hr. In the case of the UIT-treated coating, the distributions of E_r and H_r were entirely different from those before UIT, showing an obvious gradient structure characteristic. It is worth noting that both the distribution and magnitude of E_r and H_r after UIT present a similar gradient distribution tendency. As the depth away from the top surface increases within certain limits, the maximum E_r and H_r continuously decrease and then gradually reach saturation when the depth ranges beyond the thickness of the plastic deformation layer. It is evident that surface E_r and H_r have been significantly improved after UIT. The increased micro-hardness of the UIT-treated coating surface can be interpreted by the grain refinement according to the Hall–Petch relationship [50,51] and the transformation of the strengthening of the α'–martensite phase. A larger strike number N on the per unit area favors an improvement in the micro-mechanical properties of the coating surface.

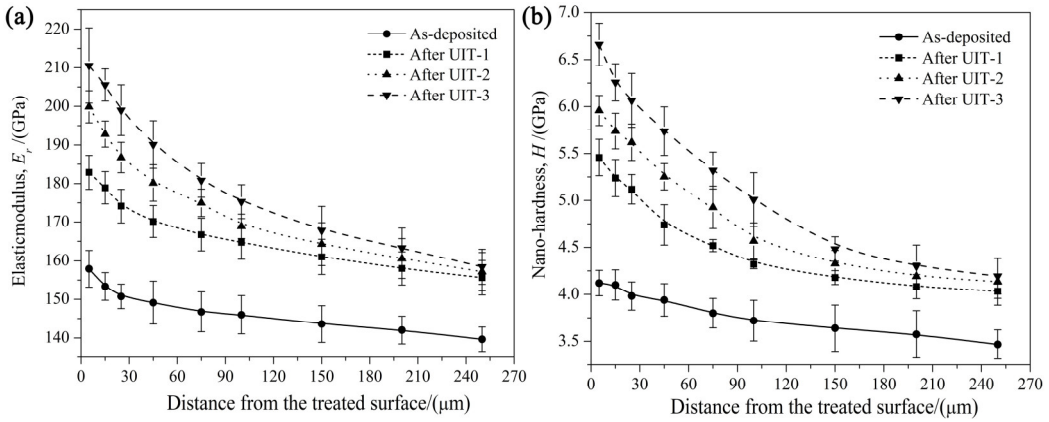

Figure 13. Comparisons of micro-mechanical properties of the coating surface: (**a**) elastic modulus; (**b**) nano-hardness.

Existing findings show that as the elastic modulus (E) and hardness (H) increase, the stiffness and wear resistance of the metal materials increase [52]. A high ratio of hardness/elastic modulus (H/E) is favorable to achieve excellent surface wear resistance [53]. Therefore, the wear resistance of the coating surface can also be evaluated by the variations in H_r/E_r before and after UIT. Here, H_r/E_r of the coating before UIT is about 0.026, and the corresponding ratios after UIT are 0.0271 (UIT–1), 0.0297 (UIT–2), and 0.0307 (UIT–3), respectively. Obviously, H_r/E_r is increased significantly after UIT. This means that the wear resistance of the coating has been improved. Meanwhile, the larger the vibration strike number on the per unit area, the higher H_r/E_r becomes. That is, the wear resistance of the coating surface can be improved with the increase in the vibration strike number. Remarkably, damage or cracks may occur on the UIT-treated coating surface as N increases beyond a reasonable level. In such a case, instead of being improved, the surface performances of the coating, including wear resistance, will degrade.

3.5. Evolution of Wear Performances and Characteristics

Figure 14 shows the variations in the friction force, friction coefficient, and wear loss before and after UIT, with the applied load changing in the range of 200 to 1000 N at a rotation speed of 380 r/min for 3 h at room temperature under oil-lubricated conditions. As shown in Figure 14, all the friction force, friction coefficient, and wear loss of the coating before and after UIT obviously increase as the applied load increases. Compared with the deposited coating before UIT, all these UIT-treated coatings are much smaller under the same test conditions. This indicates that the wear resistance of the coating has been improved after UIT. By comparing the results with different parameters, it can be also found that the friction force, friction coefficient, and wear loss obtained tend to decrease with the increase in the strike number. The higher the vibration strike number, the smaller the corresponding friction force, friction coefficient, and wear loss obtained under the same test conditions. This further demonstrates that the wear resistance of the coating has been improved as the strike number increases. The reason for this phenomenon may be the grain refinement and α'–martensitic transformation strengthening of the coating surface induced with UIT, leading to enhancements in surface hardness and wear resistance.

Figure 15 shows the wear rate before and after UIT under the applied load of 1000 N at a sliding speed of 380 r/min. As shown in Figure 15, the wear rate continues to increase as time passes. Under the applied load of 1000 N after 5 h, the wear rate of the deposited coating was about 1.466×10^{-2} g/h. Regarding the UIT-treated coating, the corresponding wear rates decreased to 0.896×10^{-2} g/h (UIT–1), 0.413×10^{-2} g/h (UIT–2), and 0.218×10^{-2} g/h (UIT–3), respectively. Obviously, the wear rates of the coating after UIT significantly reduce, keep declining, and gradually tend to slow with the strike number. This suggests that the wear resistance of the coating surface has been improved

significantly. Through the comparison and analysis, it can also be found that after being treated with UIT–3, optimal improvements in the wear resistance can be achieved in terms of the variation in the wear rate. According to the well-known Hall–Petch relationship [54], hardness is related to the grain size of the metal material. Based on the previous analysis of the microstructure evolution of the coating surface mentioned above, the improvements in hardness on the coating surface layer can be attributed to fine-grained strengthening [47]. Moreover, the formation of α'–martensitic transformation will also help to improve the hardness on the treated coating surface. In this case, the wear resistance of the coating surface has been improved considerably in the form of increased surface hardness.

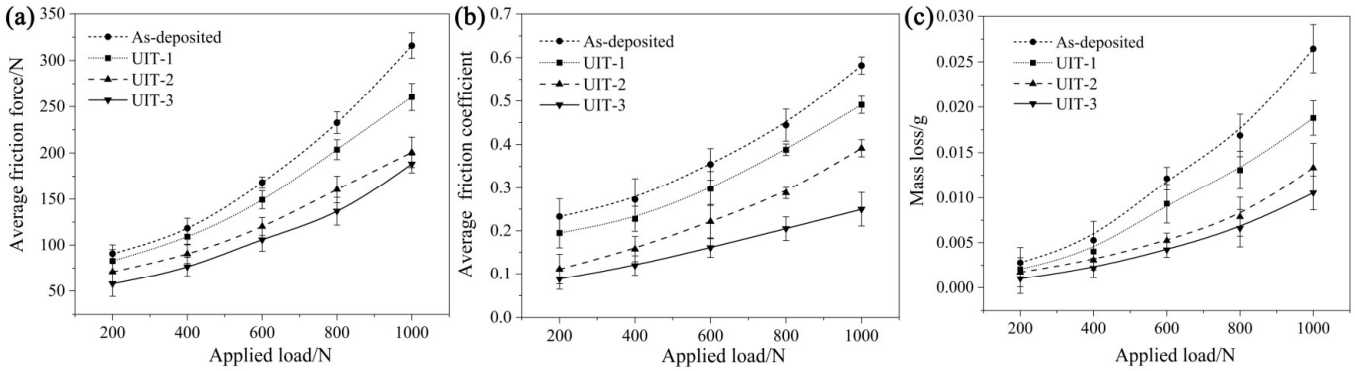

Figure 14. Comparison of the wear properties before and after UIT under different applied loads after 3 h: (**a**) friction force; (**b**) friction coefficient; (**c**) wear loss.

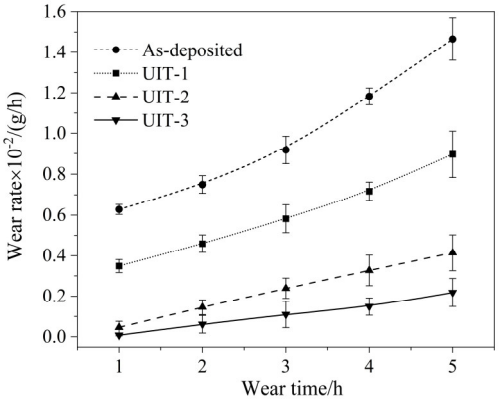

Figure 15. Variations in wear rate before and after UIT under the applied load of 1000 N.

The worn surface subjected to the applied load of 1000 N after 5 h is shown in Figure 16. Compared with the non-impacted coating, the abrasion failures of the UIT-treated coating significantly diminished, and the failure modes also changed. As shown in Figure 16a, larger areas of peelings and spots formed on the worn surface of the non-treated coating, which shows a strong adhesion wear morphology feature. When the strike number N increases to 40,000 times/mm^2, there is a small number of scaly fragments that are not fully exfoliated and are accompanied by some bright grooves parallel to the wear rotation direction produced on the worn surface of the coating, as shown in Figure 16b. This indicates that the wear form is mainly comprises fatigue spalling with a small number of furrows, and the main wear mechanism of the coating is adhesive wear combined with some abrasive wear under the effect of parameter UIT–1. As shown in Figure 16c, the amount of the lamellar peelings is reduced, and more wide and shallow furrows with some shallow flaking pits appear on the coating worn surface as the strike number N increases to 57,600 times/mm^2. This suggests that the main wear mechanism is abrasive wear accompanied by a small amount of adhesive wear under the effect of parameter UIT–2.

When the strike number N increases to 75,000 times/mm^2, a large number of micro-cuttings and furrows with uneven widths and depths are produced on the worn surface, as shown in Figure 16d. This presents the typical abrasive wear morphology, and the main failure modes are micro-cuttings and furrows under the effect of parameter UIT–3. It can clearly be seen that the wear performance of the coating surface has been improved after UIT, and the corresponding wear mechanism and failure modes also changed with the increase in the strike number N regarding per unit area.

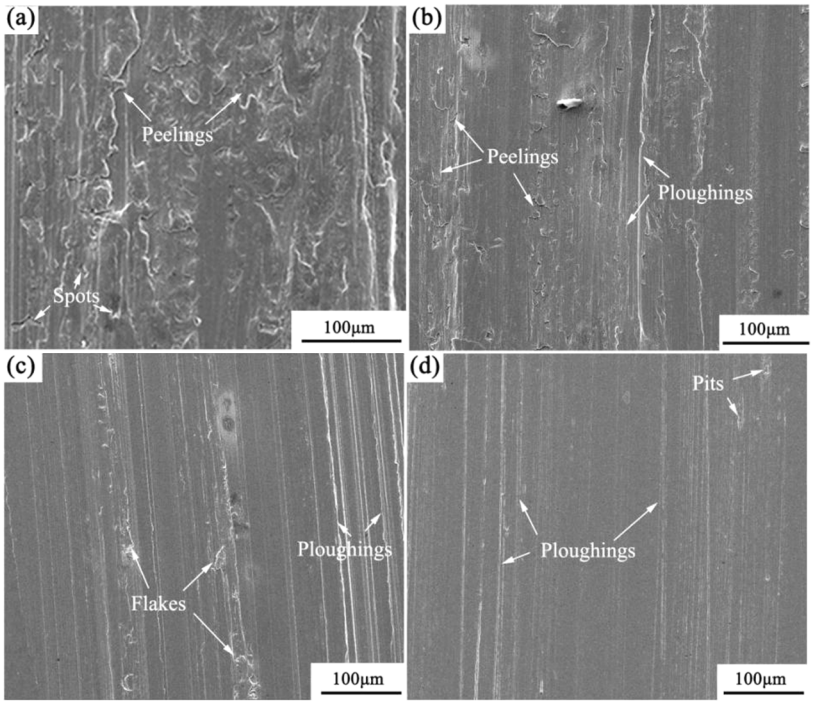

Figure 16. Worn morphologies of the coating surface under the applied load of 1000 N after 5 h: (**a**) before UIT; (**b**) after UIT–1; (**c**) after UIT–2; (**d**) after UIT–3.

4. Conclusions

In this study, a stainless steel coating was deposited and surface-modified using argon arc surfacing and a subsequent ultrasonic impact treatment. The effects of the UIT process and parameters (vibration strike number N on per area (/mm^2)) on the surface modification of the coating were investigated by comparing the surface morphology, microstructure, roughness, micro-mechanical properties, and tribological performances before and after UIT. The conclusions are as follows:

(1) The plastic deformation layer associated with an evident refined fine crystalline structure was formed on the UIT-treated coating surface. Increasing the vibration strike number, the depth of the two showed a tendency to increase and gradually reached stability.

(2) Grain refinement accompanied by the formation of a small amount of the deformation-induced α'–martensite occurred on the treated coating surface. A larger vibration strike number contributes to a higher refining effect and α'–martensite amount. After being treated at the vibration strike number of 40,000 times/mm^2 (UIT–1), 57,600 times/mm^2 (UIT–2), and 75,000 times/mm^2 (UIT–3), the average grain size decreased to 120 nm, 80 nm, and 60 nm, and the α'–martensite content reached 0.087%, 0.136%, and 0.172%, respectively.

(3) UIT can significantly improve the surface smoothness and performance of the coating. The surface roughness Ra after UIT with three vibration strike numbers decreased by 36%~74%, and the elastic modulus (Er) and micro-hardness (Hr) increased by 15.6%~33% and 19.8%~56.9%.

(4) Increasing the vibration strike number can effectively reduce the average friction coefficient and wear rate, which indicates that the wear resistance has been improved. With the increase in the vibration strike number, the wear rates are 0.896×10^{-2} g/h (UIT–1), 0.413×10^{-2} g/h (UIT–2), and 0.218×10^{-2} g/h (UIT–3), respectively. Taking the lowest wear rate as the optimization target, the vibration strike number of 75,000 times/mm^2 (UIT–3) is selected as the optimal parameter.

(5) Grain refinement strengthening and α'–martensite transformation strengthening induced with UIT contribute to the improvements in the hardness and wear resistance of the coating. The failure form changed from strong adhesive wear before UIT to adhesive wear combined with some abrasive wear after UIT-1, abrasive wear accompanied by a small amount of adhesive wear after UIT–2, and abrasive wear after UIT–3.

In summary, UIT has been found to have a high potential in modifying the surface characteristics and optimizing the mechanical performances of the deposited coating for a wide range of potential applications, including wear and corrosion. Future studies should mainly focus on the influence of UIT parameters on microstructural features such as crystallographic orientation, dislocation density, etc., and should be carried out using advanced characterization technologies, such as EBSD and high-resolution transmission electron microscopy (TEM).

Author Contributions: L.L.: conceptualization, data curation, writing—original draft preparation, and writing—review and editing; S.G.: investigation and methodology; L.J.: supervision and validation; L.Z.: investigation; J.L.: investigation and supervision; Y.G.: investigation and methodology; X.W.: supervision and validation; N.Z.: supervision and validation; H.G.: methodology and investigation; S.Z.: methodology and investigation. All authors have read and agreed to the published version of the manuscript.

Funding: This work was funded by the Excellent Talent Introduction of Shanxi Provincial Researcher Grants Program, China (No. 2022LJ023), and by the Talent Introduction Program of Taiyuan Institute of Technology (No. 2022KJ096).

Institutional Review Board Statement: Not applicable.

Informed Consent Statement: Informed consent was obtained from all subjects involved in this study.

Data Availability Statement: Data are contained within this article.

Acknowledgments: We would like to thank the Taiyuan Institute of Technology for their contribution to funding acquisition and project administration.

Conflicts of Interest: Author Jiangang Li was employed by the company China New Energy Development (Zhejiang) Co., Ltd. The remaining authors declare that the research was conducted in the absence of any commercial or financial relationships that could be construed as a potential conflict of interest.

References

1. Bolobov, V.I.; Chupin, S.A.; Akhmerov, E.V.; Plaschinskiy, V.A. Comparative Wear Resistance of Existing and Prospective Materials of Fast-Wearing Elements of Mining Equipment. *Mater. Sci. Forum* **2021**, *1040*, 117–123. [CrossRef]
2. Maher, M.; Iraola-Arregui, I.; Youcef, H.B.; Rhouta, B.; Trabadelo, V. The synergistic effect of wear-corrosion in stainless steels: A review. *Mater. Today Proc.* **2022**, *51*, 1975–1990. [CrossRef]
3. Cetin, M.; Günen, A.; Kalkandelen, M.; Karakaş, M.S. Microstructural, wear and corrosion characteristics of boronized AISI 904L superaustenitic stainless steel. *Vacuum* **2021**, *187*, 110145. [CrossRef]
4. Bildik, O.; Yaar, M. Manufacturing of Wear Resistant Iron-Steel: A Theoretical and Experimental Research on Wear Behavior. *Eng. Technol. Appl. Sci. Res.* **2021**, *11*, 7251–7256. [CrossRef]
5. Dalmau, A.; Richard, C.; Igual-Muñoz, A. Degradation mechanisms in martensitic stainless steels: Wear, corrosion and tribocorrosion appraisal. *Tribol. Int.* **2018**, *121*, 167–179. [CrossRef]
6. Gu, Y.; Xia, K.; Wu, D.; Mou, J.; Zheng, S. Technical Characteristics and Wear-Resistant Mechanism of Nano Coatings: A Review. *Coatings* **2020**, *10*, 233. [CrossRef]
7. Raghavendra, C.R.; Basavarajappa, S.; Sogalad, I.; Kumbar, V.S.; Salunkhe, P.S. Wear behavior and pin temperature of Ni-Al_2O_3 nano composite coating by electro co-deposition process. *Mater. Today Proc.* **2021**, *38*, 2162–2166. [CrossRef]

8. Lu, K.; Zhu, J.; Guo, D.; Yang, M.; Sun, H.; Wang, Z.; Hui, X.; Wu, Y. Microstructures, Corrosion Resistance and Wear Resistance of High-Entropy Alloys Coatings with Various Compositions Prepared by Laser Cladding: A Review. *Coatings* **2022**, *12*, 1023. [CrossRef]
9. Huang, B.; Zhang, C.; Zhang, G.; Liao, H. Wear and corrosion resistant performance of thermal-sprayed Fe-based amorphous coatings: A review. *Surf. Coat. Technol.* **2019**, *377*, 124896. [CrossRef]
10. Luchtenberg, P.; de Campos, P.T.; Soares, P.; Laurindo, C.A.H.; Maranho, O.; Torres, R.D. Effect of welding energy on the corrosion and tribological properties of duplex stainless steel weld overlay deposited by GMAW/CMT process. *Surf. Coat. Technol.* **2019**, *375*, 688–693. [CrossRef]
11. Zhai, W.; Bai, L.; Zhou, R.; Fan, X.; Kang, G.; Liu, Y.; Zhou, K. Recent progress on wear-resistant materials: Designs, properties, and applications. *Adv. Sci.* **2021**, *8*, 2003739. [CrossRef] [PubMed]
12. Sarila, V.K.; Koneru, H.P.; Pathapalli, V.R.; Cheepu, M.; Kantumuchu, V.C. Wear and Microstructural Characteristics of Colmonoy-4 and Stellite-6 Additive Layer Deposits on En19 Steel by Laser Cladding. *Trans. Indian Inst. Met.* **2023**, *76*, 457–464. [CrossRef]
13. Li, Z.; Yan, H.; Zhang, P.; Guo, J.; Yu, Z.; Ringsberg, J.W. Improving surface resistance to wear and corrosion of nickel-aluminum bronze by laser-clad TaC/Co-based alloy composite coatings. *Surf. Coat. Technol.* **2020**, *405*, 126592. [CrossRef]
14. Kavitha, C.; Malini, P.G.; Kantumuchu, V.C.; Kumar, N.M.; Verma, A.; Boopathi, S. An experimental study on the hardness and wear rate of carbonitride coated stainless steel. *Mater. Today Proc.* **2023**, *74*, 595–601. [CrossRef]
15. Zhang, C.; Li, S.; Lin, Y.; Ju, J.; Fu, H. Effect of boron on microstructure evolution and properties of wear-resistant cast Fe–Si–Mn–Cr–B alloy. *J. Mater. Res. Technol.* **2020**, *9*, 5564–5576.
16. Zhang, J.; Liu, J.; Liao, H.; Zeng, M.; Ma, S. A review on relationship between morphology of boride of Fe-B alloys and the wear/corrosion resistant properties and mechanisms. *J. Mater. Res. Technol.* **2019**, *8*, 6308–6320. [CrossRef]
17. Li, L.; Guo, S.; Guo, Y.; Ren, J.; Hou, W.; Wang, X.; Jia, L.; Zhang, N.; Gan, H. Effect of laser shock processing on residual stress evolution in martensitic stainless steel multi-pass butt-welded joints. *Mater. Res. Express* **2023**, *10*, 03400. [CrossRef]
18. Priyambodo, B.H.; Margono-Nugroho, K.C. Corrosion Protection on AISI 304 by Shot Peening Treatment with Variation of Particle Size and Shooting Pressure. *Mater. Sci. Forum* **2022**, *1051*, 153–159. [CrossRef]
19. Wirtz, A.; Abdulgader, M.; Milz, M.P.; Tillmann, W.; Walther, F.; Biermann, D. Thermally Assisted Machine Hammer Peening of Arc-Sprayed ZnAl-Based Corrosion Protective Coatings. *J. Manuf. Mater. Process.* **2021**, *5*, 109. [CrossRef]
20. Yıldıran Avcu, Y.; Yetik, O.; Guney, M.; Iakovakis, E.; Sınmazçelik, T.; Avcu, E. Surface, Subsurface and Tribological Properties of Ti6Al4V Alloy Shot Peened under Different Parameters. *Materials* **2020**, *13*, 4363. [CrossRef]
21. Avcu, Y.Y.; Iakovakis, E.; Guney, M.; Çalım, E.; Özkılınç, A.; Abakay, E.; Sönmez, F.; Koç, F.G.; Yamanoğlu, R.; Cengiz, A.; et al. Surface and Tribological Properties of Powder Metallurgical Cp-Ti Titanium Alloy Modified by Shot Peening. *Coatings* **2023**, *13*, 89. [CrossRef]
22. Alhussein, A.; Aouchiche, L.; Hmima, A.; Retraint, D.; Rtimi, S. Distinctive Effects of Surface Roughness and Ions Release on the Bacterial Adhesion and Inactivation of Textured Copper Oxide Surfaces. *Coatings* **2023**, *13*, 454. [CrossRef]
23. Li, L.; Zhao, S.; Zhang, N.; Guo, Y.; Gan, H. Enhanced Wear Resistance of Iron-Based Alloy Coating Induced by Ultrasonic Impact. *Coatings* **2019**, *12*, 804. [CrossRef]
24. Chen, H.; Zhang, Z.; Zhang, J.; Ji, H.; Meng, Z.; Zhang, H.; Meng, X. Effect of Ultrasonic Impact Strengthening on Surface Properties of 316L Stainless Steel Prepared by Laser Selective Melting. *Coatings* **2022**, *12*, 1243. [CrossRef]
25. Liu, C.; Lin, C.; Liu, W.; Wang, S.; Chen, Y.; Wang, J.; Wang, J. Effects of local ultrasonic impact treatment on residual stress in an engineering-scale stainless steel pipe girth weld. *Int. J. Press. Vessel. Pip.* **2021**, *192*, 104420. [CrossRef]
26. Gao, H.; Dutta, R.K.; Huizenga, R.M.; Amirthalingam, M.; Hermans, M.J.M.; Buslaps, T.; Richardson, I.M. Stress relaxation due to ultrasonic impact treatment on multi-pass welds. *Sci. Technol. Weld. Join.* **2014**, *19*, 505–513. [CrossRef]
27. Lago, J.; Trško, L.; Jambor, M.; Nový, F.; Bokůvka, O.; Mičian, M.; Pastorek, F. Fatigue Life Improvement of the High Strength Steel Welded Joints by Ultrasonic Impact Peening. *Metals* **2019**, *9*, 619. [CrossRef]
28. Zhang, H.; Wang, D.; Xia, L.; Lei, Z.; Li, Y. Effects of ultrasonic impact treatment on pre-fatigue loaded high-strength steel welded joints. *Int. J. Fatigue* **2015**, *80*, 278–287. [CrossRef]
29. Kudryavtsev, Y. Fatigue improvement of welded elements by ultrasonic impact treatment. *Exp. Appl. Mech.* **2020**, *65*, 179–190. [CrossRef]
30. Yu, Y.; He, B.; Liu, J.; Chen, Z.; Man, H. Surface plastic deformation and nanocrystallization mechanism of welded joint of 16MnR steel treated by ultrasonic impact. *Mater. Sci.* **2015**, *21*, 612–615. [CrossRef]
31. Yekta, R.T.; Ghahremani, K.; Walbridge, S. Effect of quality control parameter variations on the fatigue performance of ultrasonic impact treated welds. *Int. J. Fatigue* **2013**, *55*, 245–256. [CrossRef]
32. Yang, Y.; Jin, X.; Liu, C.; Xiao, M.; Lu, F.; Ma, S. Residual stress, mechanical properties, and grain morphology of Ti-6Al-4V alloy produced by ultrasonic impact treatment assisted wire and arc additive manufacturing. *Metals* **2018**, *8*, 934. [CrossRef]
33. Li, Q.; Wang, H.; Che, C.; Wan, L.; Dong, X.; Wang, S.; Zhang, C. Effect of ultrasonic impact on the organization and friction wear performance of AZ31B magnesium alloy micro-arc oxidation composite coating. *Coatings* **2023**, *13*, 1161. [CrossRef]
34. Li, M.; Zhang, Q.; Han, B.; Song, L.; Li, J.; Zhang, S. Effects of ultrasonic impact treatment on structures and properties of laser cladding Al0.5CoCrFeMnNi high entropy alloy coatings. *Mater. Chem. Phys.* **2021**, *258*, 123850. [CrossRef]

35. *GB/T 3077-2015*; Alloy Structure Steels. In General Administration of Quality Supervision, Inspection and Quarantine of the People's Republic of China, Standardization Administration of the People's Republic of China. Standards Press of China: Beijing, China, 2015.
36. *EN ISO 683-1*; Heat-Treatable Steels, Alloy Steels and Free-Cutting Steels—Part 1: Non-Alloy Steels for Quenching and Tempering. International Organization for Standardization: Geneva, Switzerland, 2018.
37. Yang, X.; Wang, X.; Ling, X.; Wang, D. Enhanced mechanical behaviors of gradient nano-grained austenite stainless steel by means of ultrasonic impact treatment. *Results Phys.* **2017**, *7*, 1412–1421. [CrossRef]
38. Monshi, A.; Foroughi, M.R.; Monshi, M.R. Modified Scherrer equation to estimate more accurately nano-crystallite size using XRD. *World J. Nano Sci. Eng.* **2012**, *2*, 154–160. [CrossRef]
39. *ISO 4287*; Geometrical Product Specifications (GPS), Surface Texture: Profile Method, Terms, Definitions and Surface Texture Parameters. International Organization for Standardization: Geneva, Switzerland, 1997.
40. Huang, H.; Li, J.; Li, D.; Liu, R.; Lei, G.; Huang, Q.; Yan, L. TEM, XRD and nanoindentation characterization of Xenon ion irradiation damage in austenitic stainless steels. *J. Nucl. Mater.* **2014**, *454*, 168–172. [CrossRef]
41. Zhou, X.; Li, L.; Wen, D.; Liu, X.; Wu, C. Effect of hybrid ratio on friction and wear behavior of AZ91D matrix nanocomposites under oil lubricated conditions. *Trans. Nonferrous Met. Soc. China* **2018**, *28*, 440–450. [CrossRef]
42. Li, L.; Kim, M.; Lee, S.; Bae, M.; Lee, D. Influence of multiple ultrasonic impact treatments on surface roughness and wear performance of SUS301 steel. *Surf. Coat. Technol.* **2016**, *307*, 517–524. [CrossRef]
43. Vasylyev, M.A.; Mordyuk, B.N.; Sidorenko, S.I.; Voloshko, S.M.; Burmak, A.P. Influence of microstructural features and deformation-induced martensite on hardening of stainless steel by cryogenic ultrasonic impact treatment. *Surf. Coat. Technol.* **2018**, *343*, 57–68. [CrossRef]
44. Mao, X.; Sun, J.; Feng, Y.; Zhou, X.; Zhao, X. High-temperature wear properties of gradient microstructure induced by ultrasonic impact treatment. *Mater. Lett.* **2019**, *246*, 178–181. [CrossRef]
45. Wang, C.; Li, R.; Bi, X.; Yuan, W.; Gu, J.; Chen, J.; Yan, M.; Zhang, Z. Microstructure and wear resistance property of laser cladded CrCoNi coatings assisted by ultrasonic impact treatment. *J. Mater. Res. Technol.* **2023**, *22*, 853–864. [CrossRef]
46. Kahraman, F.; Kahraman, H.; Yolcu, C.; Ayça, D.K. Wear behavior of ultrasonic impact treated S235JR steel. *Mater. Test.* **2017**, *59*, 445–449. [CrossRef]
47. Wang, G.; Lei, M.; Guo, D. Interactions between surface integrity parameters on AISI 304 austenitic stainless steel components by ultrasonic impact treatment. *Procedia CIRP* **2016**, *45*, 323–326. [CrossRef]
48. Yasuoka, M.; Wang, P.; Zhang, K.; Qiu, Z.; Kusaka, K.; Pyoun, Y.S.; Murakami, R. Improvement of the fatigue strength of SUS304 austenite stainless steel using ultrasonic nanocrystal surface modification. *Surf. Coat. Technol.* **2013**, *218*, 93–98. [CrossRef]
49. Wang, H.; Song, G.; Tang, G. Effect of electropulsing on surface mechanical properties and microstructure of AISI 304 stainless steel during ultrasonic surface rolling process. *Mater. Sci. Eng. A* **2016**, *662*, 456–467. [CrossRef]
50. Amanov, A.; Berkebile, S.P. Enhancement of sliding wear and scratch resistance of two thermally sprayed Cr-based coatings by ultrasonic nanocrystal surface modification. *Wear* **2023**, *512*, 204555. [CrossRef]
51. He, B.; Yu, Y.; Xia, S.; Lv, Z.M. Effect of ultrasonic impact treating on wear resistance and microhardness of AZ91D magnesium alloy. *Rare Met. Mater. Eng.* **2017**, *46*, 17–22.
52. Luo, K.; Lu, J.; Zhang, Y.; Zhou, J.; Zhang, L.; Dai, F.; Zhang, L.; Zhong, J.; Cui, C. Effects of laser shock processing on mechanical properties and micro-structure of ANSI 304 austenitic stainless steel. *Mater. Sci. Eng. A* **2011**, *528*, 4783–4788. [CrossRef]
53. Leyland, A.; Matthews, A. On the significance of the H/E ratio in wear control: A nanocomposite coating approach to optimised tribological behaviour. *Wear* **2000**, *246*, 1–11. [CrossRef]
54. Amanov, A.; Penkov, O.V.; Pyun, Y.S.; Kim, D.E. Effects of ultrasonic nanocrystalline surface modification on the tribological properties of AZ91D magnesium alloy. *Tribol. Int.* **2012**, *54*, 106–113. [CrossRef]